Sintering Forces Acting among Particles during Sintering by Grain Boundary/Surface Diffusion

Fumihiro Wakai[1], Olivier Guillon[2], Gaku Okuma[1], Norimasa Nishiyama[1]

[1] Laboratory for Materials and Structures, Institute of Innovative Research, Tokyo Institute of Technology, R3-23 4259 Nagatsuta, Midori, Yokohama, 226-8503, Japan
[2] Institute of Energy and Climate Research IEK-1: Materials Synthesis and Processing. Forschungszentrum Jülich GmbH, D-52425 Jülich, Germany

Abstract

The microstructural evolution during sintering involves the formation and pinch-off of pore channels. The sintering of three particles in three dimensions is a simple model for studying the pinch-off of a pore channel. We simulate the solid-state sintering of three particles by using Brakke's Surface Evolver program, which incorporates coupled grain boundary diffusion and surface diffusion. The pinch-off of pore channel divides the sintering process into two stages; the initial stage and the later stage. The contact area has a non-circular shape bounded by both surface triple junction and triple junction in the later stage. A general method is presented to determine the sintering force acting on the non-circular contact. The mechanical approach of densification, where the relative motion of particles is driven by both sintering force and applied force, is applicable not only for the initial stage, but also for the later stage.

Keywords: Sintering; Simulation; Micromechanical Modeling

***** Corresponding author.
Tel.: +81-45-924-5361; fax: +81-45-924-5390.
E-mail address: wakai.f.aa@m.titech.ac.jp (F. Wakai)

1 INTRODUCTION

Controlling the shrinkage and microstructural evolution during sintering is crucial to the dimensional accuracy and properties of products. However, it is difficult to predict the sintering behavior with accuracy, because macroscopic shrinkage depends on the detail of local geometry at the particle scale. The densification in solid-state sintering of crystalline particles involves motion normal to the boundary of two adjacent grains, in a similar way to diffusional creep either by bulk diffusion [1, 2] or by grain boundary diffusion [3]. Even without the applied stress, the shrinkage in sintering occurs spontaneously by diffusive transport of matter driven by surface tension at temperatures below the melting point. Beere [4], Riedel, Zipse and Svoboda [5], Wakai and Brakke [6] defined the thermodynamic driving force of solid-state sintering, i.e., the sintering force, acting on a circular contact between two particles. The sintering force is also defined for viscous sintering of glass particles.[7] This mesoscopic force at the particle scale is the origin of macroscopic sintering stress tensor either isotropic [8, 9] or anisotropic [10] in continuum mechanics of sintering, where the macroscopic shrinkage rate is expressed as a response to the applied stress and the sintering stress.[5, 11-14] The continuum mechanics is useful for predicting the dimensions of final sintered products,[14]

and for analyzing problems of constrained sintering [12] and co-sintering.

The center-to-center approach of two particles and the neck growth were major topics in the classical theory of sintering which was developed by Frenkel [15], Kuczynski [16], and Kingery and Berg [17]. Coble [18] and Johnson [19] analyzed the role of grain boundary diffusion. Bross and Exner [20] and Swinkels and Ashby [21] included the coupling of grain boundary diffusion and surface diffusion. In recent years, several techniques for the computer simulation of solid-state sintering have been developed, including finite difference method (FDM) [20, 22-24], finite element method (FEM) [25-30], Monte Carlo Potts models (MC) [31-34], phase field approaches (PH) [35-37], discrete element method (DEM) [38-43] and Surface Evolver program [6, 44, 45].

The naturally evolving pore structure during sintering is characterized by the formation and pinch-off of pore channels [46]. Consider sintering of three spherical particles in three dimensions (Fig. 1 (a)). There is a pore channel at the center of three particles. The lower part shows a circular contact in the initial stage. As these contact areas expand, the radius of the pore channel decreases, and the contact has a non-circular shape in Fig. 1 (c). When the pore channel is pinched off, a triple junction, where three grain boundaries

meet, is formed as shown in Fig. 1 (d) and (e). As a model of pore channel pinch-off, we analyzed the solid-state sintering of three particles by coupled grain boundary diffusion and surface diffusion. We show the sintering force can be defined for non-circular contacts bounded by both surface triple junction and triple junction.

The introduction of the concept of sintering force confers an advantage in analyzing the effect of applied force on densification as will be described in Section 5.1. The relative motion of particles depends on both sintering force and mechanical force transmitted by the contact area.[5, 13, 38, 41] It is the microscopic principle for the enhanced densification by sinter-forging, hot pressing, hot isostatic pressing, and spark plasma sintering. On the other hand, the debonding occurs by a tension force, which is larger than the sintering force, leading to the formation of defects. The knowledge on sintering force among interacting multiple particles will be useful to understand the micromechanics in the intermediate stage of sintering.

2 THEORY

2.1 Grain boundary diffusion

We consider the grain boundary diffusion in a non-circular contact shown in Fig. 1 (e), lower part. The grain boundary

intersects with the surface to form a surface triple junction C_1 (free surface-grain boundary-free surface). The vacancy diffuses from the source (surface near the surface triple junction) to the sink (grain boundary). The chemical potential of atoms on a flat grain boundary depends on normal traction σ_n on the boundary.[2] The flux along grain boundary is proportional to the gradient of chemical potential, then, the gradient of normal stress. The normal stress distribution is a solution of Poisson's equation [5, 19]

$$\nabla_s^2 \sigma_n = -\frac{kT}{\Omega \delta D_{gb}} \dot{u}_n \quad \text{on } A \tag{1}$$

where ∇_s^2 denotes the surface Laplacian, $\dot{u}_n$ is the relative velocity between two particles, Ω is the atomic volume, δD_{gb} is the grain boundary diffusion times the grain boundary thickness, k is Boltzmann's constant, and T is absolute temperature.

We solve Eq. (1) for a contact of any shape with the boundary condition along the surface triple junction C_1 and triple junction C_2 in Fig. 1 (e). The chemical potential of atoms on the surface depends on surface tension $\gamma_s \kappa$, where γ_s is the surface energy, and κ is the curvature. At the surface triple junction, the chemical potential on the surface is equal to that on the grain boundary, then,

$\sigma_n = \gamma_s \kappa$ on C_1 (surface triple junction) (2)

where the sign of curvature is negative for a spherical particle. The boundary condition along the triple junction is zero from symmetry

$\frac{\partial \sigma_n}{\partial \nu} = 0$ on C_2 (triple junction) (3)

where $\partial/\partial\nu$ is a directional derivative in the direction of the unit vector tangential to the contact plane and normal to the triple junction, drawn outward from the region enclosed by C_1 and C_2. When external force is not applied, the integration of the normal stress over the boundary area A must balance with the surface tension force along the circumference.[19] By including both surface tension and grain boundary tension (see Fig.1 (e), upper part), the force balance is expressed as

$$\int_A \sigma_n dS = -\gamma_s L_1 \sin(\psi/2) - \frac{1}{2}\gamma_{gb} L_2 \sin(\pi/3) \quad (4)$$

where L_1 and L_2 are length of surface triple junction and that of triple junction, respectively. The grain boundary tension term is multiplied by 1/2, because it is shared by two particles. The equilibrium dihedral angle ψ is given by the ratio of the grain boundary energy γ_{gb} to the surface energy γ_s

$$\gamma_{gb} = 2\gamma_s \cos(\psi/2). \quad (5)$$

Here, we give the relationship between the relative velocity $\dot{u}_n$ and the sintering force. Green's second identity for a surface A is

$$\int_A \left(\phi \nabla_s^2 \varphi - \varphi \nabla_s^2 \phi\right) dS = \int_C \left(\phi \frac{\partial \varphi}{\partial \nu} - \varphi \frac{\partial \phi}{\partial \nu}\right) ds . \quad (6)$$

Now choose

$$\varphi = \sigma_n \quad (7)$$

$$\nabla_s^2 \phi = -1 \text{ on } A \text{ (contact area)} \quad (8)$$

$$\phi = 0 \text{ on } C_1 \text{ (surface triple junction)} \quad (9)$$

$$\frac{\partial \phi}{\partial \nu} = 0 \text{ on } C_2 \text{ (triple junction)} \quad (10)$$

and apply to the contact area. We obtain

$$-\frac{kT}{\Omega \delta D_{gb}} \dot{u}_n \int_A \phi dS + \int_A \sigma_n dS = -\int_{C_1} \gamma_s \kappa \frac{\partial \phi}{\partial \nu} ds \ . \quad (11)$$

By substituting Eq. (4) into Eq. (11), the relative velocity is given by

$$\dot{u}_n = -F^s / K' \quad (12)$$

$$F^s = \gamma_s \kappa^* A + \gamma_s L_1 \sin(\psi/2) + \frac{1}{2} \gamma_{gb} L_2 \sin(\pi/3) \quad (13)$$

$$K' = \frac{kT}{\Omega \delta D_{gb}} g^* A^2 \quad (14)$$

where F^s is the sintering force, K' is the effective viscosity, and A is the contact area. κ^* is a weighted average of curvature at surface triple junction

$$\kappa^* = -\frac{1}{A} \int_{C_1} \kappa \frac{\partial \varphi}{\partial \nu} ds . \quad (15)$$

g^* is a geometry factor that depends on the shape of contact area

$$g^* = \frac{1}{A^2}\int_A \varphi dS . \tag{16}$$

ϕ has the dimension of area. For sintering of two identical spheres, the contact area is a circle of radius c, then, $\phi = \left(c^2 - r^2\right)/4$ in two-dimensional polar coordinates, $g^* = 1/8\pi$, and $\kappa^* = \kappa_{neck}$ where κ_{neck} is the curvature at the neck. The sintering force on a circular contact agrees with the previous analyses [4, 5]

$$F^s = \gamma_s \kappa_{neck} \pi c^2 + 2\pi c \gamma_s \sin\left(\psi/2\right). \tag{17}$$

3.2 Surface diffusion

The surface motion occurs by atoms moving along the surface as analyzed by Mullins,[47]

$$\upsilon_n = -\frac{\gamma_s \Omega \delta D_s}{kT}\nabla_s^2 \kappa \ . \tag{18}$$

where δD_s is the surface diffusion coefficient. The normal velocity υ_n is proportional to the negative of the surface Laplacian of the mean curvature.[48] The diffusive flux along the surface j_s and that along the grain boundary j_{gb} must be continuous at the surface triple junction

$$j_{gb} = 2 j_s . \tag{19}$$

3 SIMULATION METHOD

Brakke's Surface Evolver program [44] was used to simulate the sintering of three particles of the same size by coupled grain boundary/surface diffusion. The details of the simulation method are described elsewhere,[6] then, we describe it briefly. We assumed the isotropic surface energy and the isotropic grain boundary energy. The stress distribution in the flat grain boundary and ϕ are determined by solving Eq. (1) and Eq. (8) by using the finite element method, respectively. The sintering force and the effective viscosity are determined to give the relative velocity $\dot{u}_n$. In each time step Δt, vertices on each particle surface are shifted $\dot{u}_n \Delta t / \sqrt{3}$ toward the center of three particles. The contact area was expanded by moving vertices along the surface triple junction, so as to satisfy the continuity condition, Eq. (19). This motion is proportional to the diffusive flux j_{gb} along the surface triple junction.

4 RESULTS

4.1 Total energy and neck growth

The growth of contact area, i.e., neck growth, decreases the sum of energies associated with the surface area A_s and the grain boundary area A_{gb}

$$E = \gamma_s A_s + \gamma_{gb} A_{gb}. \quad (20)$$

Here we define the normalized energy per particle as

$$\Delta E^* = \left(E - 3E_0\right)/3E_0 \quad (21)$$

where $E_0 = \gamma_s 4\pi r_0^2$ is the energy of a single sphere with a radius of r_0. The energy is plotted in Fig. 2 as a function of the dimensionless time

$$t^* = \frac{\gamma_s \Omega \delta D_s}{kTr_0^4} t. \quad (22)$$

which is defined for the sintering by surface diffusion according to Herring's scaling law[49]. The three particles reach the final equilibrium shape with the minimal energy as shown in Fig. 2. The equilibrium energy of a ring of three particles depends on γ_{gb}/γ_s as analyzed by Kellet and Lange [50] and Wakai (Fig.3 in [51]).

The increase of contact area is expressed as the growth of effective contact radius

$$c^* = \sqrt{A/\pi} \ . \quad (23)$$

It is plotted as a function of dimensionless time in Fig. 3 (a) and (b). The neck growth in the initial stage of sintering is expressed as [52]

$$\left(c^*/r_0\right)^m = \beta t^* \qquad (24)$$

where m and β are numerical exponents. The value of m is about 6 for both grain boundary diffusion [18, 19] and surface diffusion [53, 54]. This relationship is only valid in the very beginning of the initial stage. After the pore channel is pinched off (filled black circles in Fig. 3), the value of m increases with time. The effective contact radius at the pinch-off is close to $c^*/r_0 = 0.5$, and depends on γ_{gb}/γ_s and $\delta D_{gb}/\delta D_s$, because these factors affect the shape of contacts just before the pinch-off (Fig. 1 (c)).

4.2 Effective viscosity and geometry factor

The effective viscosity, Eq. (14), is inversely proportional to both the grain boundary diffusion coefficient and the geometry factor g^*, and increases with the fourth power of the effective contact radius. The geometry factor g^* defined by Eq. (16) is a coefficient which describes the effect of contact shape on the effective viscosity. Figure 4 shows the relationship between the geometry factor and the effective contact radius. The geometry factor is independent of contact

area, but depends only on its shape. It is constant ($1/8\pi$) as long as the contact shape is circular. As the triple junction is formed, the shape becomes non-circular. The increase of the geometry factor shows the effect of non-circular contact in the later stage.

4.3 Sintering force

The grain boundary diffusion is driven by stress distribution in the contact area as illustrated in Fig. 1, lower part. For a circular contact area (Fig. 1 (a), (b)), the stress is tension at the neck surface, and compression at the center of the contact. The stress distribution is parabolic

$$\sigma_n = 2\left(\gamma_s \kappa_{neck} - \bar{\sigma}_n\right)\left((r/c)^2 - 1\right) + \gamma_s \kappa_{neck} \qquad (25)$$

where r is the distance from the center of the contact, and $\bar{\sigma}_n$ is the average normal stress, which arises from Eq. (4),

$$\bar{\sigma}_n = -\frac{\gamma_s}{c}\sin\left(\frac{\psi}{2}\right). \qquad (26)$$

It is negative, and the compressive stress is very large at small contact radius. The difference between $\bar{\sigma}_n$ and the tensile stress $\gamma_s \kappa_{neck}$ at the neck surface ($r = c$) is the origin of the sintering force for a circular contact

$$F^s = \left(\gamma_s \kappa_{neck} - \bar{\sigma}_n\right) A \ . \qquad (27)$$

As the radius of pore channel decreases, the curvature near the pore channel increases significantly (Fig. 1 (c)), and the local curvature becomes very large just after the pinch-off (Fig. 1 (d)). The sintering force of non-circular contact, where neck curvature depends on position, is calculated by substituting the weighted average of curvature κ^* (Eq. (15)) for κ_{neck} in Eq. (27).

Figure 5 shows the weighted average of curvature decreases with increasing the effective contact radius. κ^* shows a small peak at the pinch-off of pore channel, and reaches to an equilibrium value in the final state. κ^* in the initial stage decreases with increasing γ_{gb}/γ_s (Fig. 5 (a)). This result is consistent with the geometrical analysis of Johnson [19] and Coblenz [52]. κ^* in the initial stage decreases with decreasing $\delta D_{gb}/\delta D_s$ in Fig. 5 (b), because so-called "undercutting" reduce the neck curvature when the surface diffusion is dominant as analyzed by Nichols and Mullins.[53, 54]

The sintering force is calculated by Eq. (13), and is plotted as a function of effective contact radius in Fig. 6 (a), (b). It varies slightly showing a broad peak in the initial stage. After showing a sharp peak at pinch-off of pore channel, it

decreases to zero at the equilibrium. The sintering force depends on γ_{gb}/γ_s and $\delta D_{gb}/\delta D_s$, because it is a function of κ*.

4.4 Shrinkage

The relative velocity $\dot{u}_n$ (Eq. (12)) is given by the effective viscosity and the sintering force, and the relation between relative velocity and effective contact radius is shown in Fig. 7. The relative velocity increases proportionally to $\delta D_{gb}/\delta D_s$. The slope of line in the double-logarithmic plot was about 4 in the initial stage. The sintering force can be regarded as constant in the initial stage, so that the relative velocity depends mainly on the effective viscosity, which is proportional to the fourth power of the contact radius. A small peak on the velocity curve shows the pinch-off of pore channel. The decrease of sintering force is responsible for the decrease of relative velocity in the later stage. The relative motion of particles stops when the sintering force becomes zero finally.

The shrinkage in sintering is defined by the distance R between mass centers of two particles as shown in Fig. 1 (a), upper part. The mass center of a particle was calculated from a surface integral of position by using the divergence theorem of Gauss.[6] The shrinkage $\Delta R = R - 2r_0$ is plotted as a function

of the dimensionless time in Fig. 8. The shrinkage u by rigid body motion is given by integrating relative velocity $\dot{u}_n$. The grain boundary diffusion is very efficient, so that 83 % of the final shrinkage is caused by the rigid body motion at $\delta D_{gb}/\delta D_s = 1$. Especially, the grain boundary diffusion is fully responsible for the shrinkage in the initial stage, even in the case of $\delta D_{gb}/\delta D_s$ = 0.1. The motion of mass center of a particle occurs by both rigid body motion and shape change by surface diffusion. The difference between ΔR and u in the later stage is caused by surface diffusion. Since the sintering by surface diffusion can take place without grain boundary diffusion, the shift of mass center occurs even at $\delta D_{gb}/\delta D_s$ = 0. Although the sintering force is defined also at $\delta D_{gb}/\delta D_s$ = 0 in Fig. 7 (b), the shrinkage u by rigid body motion is zero, because the effective viscosity is infinitely large.

The pinch-off of pore channel divides the sintering process into only two stages; the initial stage with open pore channel and the later stage without internal porosity. The slope of shrinkage curves (u) for $\delta D_{gb}/\delta D_s$ = 1 and 0.1 in Fig. 8 changes at the pinch-off. By assuming an appropriate geometrical relation between the relative velocity and the neck growth rate,

Coble [18] obtained a relation between u and the dimensionless time for the initial stage of sintering of two particles

$$u \propto t^{*n} \tag{28}$$

where n is an exponent. In the initial stage, the slope of shrinkage curve was close to the value n = 1/3 as proposed by Coble. The value of n decreased in the later stage in the present simulation. The initial stage of sintering ends with the pinch-off of pore channel in a very short period of time. The amount of shrinkage during the initial stage is only 20 % of the total shrinkage u by rigid body motion. The shrinkage continues in the later stage, which lasts for a long time.

5 DISCUSSION

5.1 Effect of applied force on densification

The relative velocity between two adjoining particles is expressed as

$$\dot{u}_n = \frac{\Omega \delta D_{gb}}{kTg^* A^2}\left(F_n - F^s\right) \tag{29}$$

where F_n is the force transmitted by the contact area. This is the approach used by Jagota and Dawson [38], Parhami and McMeeking [41], McMeeking and Kuhn [13], Riedel, Zipse and Svoboda[5] for circular contacts. Eq. (29) is a generalized form applicable also to non-circular contacts. It shows that the sintering force is equivalent to the tension force necessary

to stop the shrinkage ($\dot{u}_n = 0$) as defined by Gregg and Rhines.[56] This equation shows also that the debonding occurs by the application of tension force, which is larger than the sintering force.

The discrete element method (DEM), which was initially developed for granular materials,[57] has been applied to sintering, in which the motion of a huge number of spherical particles is simulated by using the micromechanical relation of Eq. (29). The sintering force used in DEM simulation was derived from the analysis of viscous flow,[38-41] the initial stage of solid-state sintering,[42] and the periodic porous structures in equilibrium.[43] Bouvard and McMeeking [24] simulated the effect of applied force on sintering of two particles by coupled grain boundary and surface diffusion, and proved that the shrinkage rate was the sum of free sintering rate and the creep rate by the applied force. Martin [42, 58, 59] used a convenient approximate formulation of free sintering rate, which was provided by Bouvard and McMeeking, in their DEM simulation of sintering. In their formulation the sintering force was approximately expressed as a constant [58] or a linear function of contact radius.[42] By following their approximate approach, the sintering force is schematically illustrated in Fig. 9, where parameters (F_1^s, c_1*, c_2*) are chosen according to

the simulation results in Fig. 6 (a) and (b). The sintering force can be considered constant before the pinch-off at c_1*, and decreases linearly to zero at the equilibrium c_2*. For the sintering of three particles, the contact radius at the pinch-off c_1* is about 0.5, and the equilibrium contact radius c_2* is calculated from the dihedral angle [50, 51]. The authors suppose this formulation can be used for DEM simulation of the later stage of sintering.

This two-part piece-wise linear approximation is simple, and can be generalized to other configurations of pore channel. Kellett and Lange [50] modeled the pore channel by using closed arrays, or rings, of spherical particles. The number of particle n is the coordination number of the pore channel. The spheres are located at vertices of regular polygon. The pinch-off takes place when the sphere surface touch the center of the polygon as shown in Fig. 10. The contact radius depends on the geometry

$$c_1^* = r_0 \sin\theta \tag{30}$$

where the angle is $\theta = (n-2)\pi/2n$. The contact radius at the pinch-off increases with increasing the pore coordination number; it is c_1^*/r_0= 0.71 and 0.81 for $n=4$ and $n=5$, respectively. The sintering force can be considered constant

even for large contact radius $c^*/r_0 > 0.5$, when the coordination number of pore channel is larger than three.

The sintering force depends on the weighted average of curvature along the surface triple junction. Since the local curvature becomes very large at the pinch-off, we suppose that the sharp peak in sintering force will be also observed for pore channels with the coordination number larger than three. Although this effect gives a small peak in relative velocity in Fig. 7, its contribution to the total shrinkage is very little (Fig. 8), because the very narrow pore channel disappears quickly at the pinch-off. Therefore, for simplicity, it is appropriate to use the two-part piece-wise linear approximation for the sintering force (Fig. 9).

5.2 Motion of mass center by surface diffusion

Several diffusion mechanisms contribute to sintering concurrently, and their relative importance varies with temperature and particle size.[21] In this paper, we analyzed the sintering force in solid-state sintering by coupled grain boundary diffusion and surface diffusion, which is the most important mechanism for the densification of fine crystalline particles. Swinkels and Ashby [21] distinguished "densifying mechanisms", where the grain boundary acts as sink/source of vacancy, from "non-densifying mechanisms", where only the

surface acts as source/sink of matter transport. However, the mass center of a particle shifts with time by non-densifying mechanisms, because the particle shape changes by surface diffusion, bulk diffusion, and evaporation-condensation. In the present paper, we showed that the motion of mass center by surface diffusion is important in the later stage, especially, when the grain boundary diffusion coefficient is lower than the surface diffusion coefficient (Fig. 8). Here we point out that a thermodynamic driving force can be defined for the motion of mass center by surface diffusion.[6] Furthermore, the surface motion is controlled by the interface reaction when the surface diffusion is infinitely fast compared with the attachment kinetics.[47, 48] The sintering by interface controlled surface diffusion is described mathematically in a similar way with that by evaporation-condensation process.[60] One of the authors has analyzed the sintering force [45, 61] and the moment of inertia tensor,[62] which characterizes the shape evolution, in the interface controlled sintering of three particles also. The sintering force increased with time in the initial stage, showed a sharp peak at the pinch-off of pore channel, and decreased to zero at the equilibrium. These features observed during the pinch-off of pore channel were common in both the densifying mechanism and non-densifying mechanisms.

5.3 Initial stage of sintering in various simulation models

Computer simulations were carried out to study the initial stage of solid-state sintering of two particles for several decades. Many aspects of the results of each of these investigations [23-30] lie in quantitative agreement with one another and with analytical models.[52] For example, all of the simulation models yield a value of 6 for the exponent m of Eq. (24), and they find that the shrinkage takes on a power-law form of Eq. (28). In most cases, the differences between the simulations and the analytical models lie on the assumption of the neck shape that depends on γ_{gb}/γ_s and $\delta D_{gb}/\delta D_s$.[63-64]

The initial stage of sintering of three particles in three dimensions is essentially the same with that of two particles, especially at the very beginning. The present results on three particles agreed well with our previous results on two particles.[6] On the other hand, Tikare, Braginsky and Olevsky [31] studied the sintering of three particles in two dimensions by using Monte Carlo simulation. Since a closed pore was formed at the beginning, their two-dimensional model was able to study the final stage, where the closed pore shrank. While real samples possess several types of pores, the sintering of four particles will be a simple model for investigating the formation and shrinkage of a closed pore in three dimensions.

6 CONCLUSION

The implementation of the finite element method to analyze the stress distribution on grain boundary in Brakke's Surface Evolver program allows this method to be extended to the simulation of sintering by coupled grain boundary diffusion and surface diffusion. Consequently, the calculation of sintering force acting on a contact of any shape becomes tractable, from which the constitutive law for the relative velocity between two adjoining particles can be extracted. The evolution in the sintering of three particles leads to the pinch-off of pore channel, and the constitutive law was applicable to both the initial stage and the later stage after the pinch-off. This simulation algorithm will help to analyze the interaction of many particles in solid-state sintering.

ACKNOWLEDGMENTS

FW thanks DFG support as a Mercator Fellowship (within Priority Program 1959). This work was supported by JSPS KAKENHI Grant Number JP26249110.

REFERENCES

1 Nabarro FRN. Deformation of crystals by the motion of single ions. In: Bristol Conf. on Strength of Solids. 1948; p. 75-90.

2 Herring C. Diffusional viscosity of a polycrystalline solid. J Appl Phys. 1950;21:437-445.

3 Coble RL. A model for boundary diffusion controlled creep in polycrystalline materials. J Appl Phys. 1963;34:1679-1682.

4 Beere W. The second stage sintering kinetics of powder compacts. Acta Metall. 1975;23:139-145.

5 Riedel H, Zipse H, Svoboda J. Equilibrium pore surfaces, sintering stresses and constitutive equations for the intermediate and late stages of sintering-II. Diffusional densification and creep. Acta Metall Mater. 1994;42:445-452.

6 Wakai F, Brakke K. Mechanics of sintering for coupled grain boundary and surface diffusion. Acta Mater. 2011;59:5379-5387.

7 Wakai F, Katsura K, Kanchika S, Shinoda Y, Akatsu T, Shinagawa K. Sintering force behind the viscous sintering of two particles, Acta Mater. 2016;109:292-299.

8 Svoboda J, Riedel H, Zipse H. Equilibrium pore surfaces, sintering stresses and constitutive equations for the intermediate and late stages of sintering-I. computation of equilibrium surfaces. Acta Metall Mater. 1994;42:435-443.

9 Wakai F, Shinoda Y, Akatsu . Method to calculate sintering stress of porous materials in equilibrium. Acta Mater. 2004;52:5621-5631.

10 Wakai F, Shinoda Y. Anisotropic sintering stress for sintering of particles arranged in orthotropic symmetry. Acta Mater. 2009;57:3955-3964.

11 Jagota A, Dawson PR, Jenkins JT. An anisotropic continuum model for the sintering and compaction of powder packings. Mech Mater. 1988;7:255-269.

12 Bordia RK, Scherer GW. On constrained sintering-I. constitutive model for a sintering body. Acta Metall Mater. 1988;36:2393-2397.

13 McMeeking RM, Kuhn LT. A diffusional creep law for powder compacts. Acta Metall Mater. 1992;40:961-969.

14 Olevsky EA. Theory of sintering: from discrete to continuum. Mater Sci Eng. R 1998;23:41-100.

15 Frenkel J. Viscous flow of crystalline bodies under the action of surface tension. J Phys USSR. 1945;9:385-391.

16 Kuczynski GC. Self-diffusion in sintering of metallic particles. Trans Am Inst Min Metall Eng. 1949;185:169-178.

17 Kingery WD, Berg M. Study of the initial stages of sintering solids by viscous flow, evaporation-condensation, and self-diffusion. J Appl Phys 1955;26:1205-1212.

18 Coble RL. Initial sintering of alumina and hematite. J Am Ceram Soc. 1958;41:55-62.

19 Johnson DL. New method of obtaining volume, grain-boundary, and surface diffusion coefficients from sintering data. J Appl Phys. 1969;40:192-200.

20 Bross P, Exner HE. Computer simulation of sintering processes. Acta Metall. 1979;27:1013-1020.

21 Swinkels FB, Ashby MF. A second report on sintering diagrams. Acta Metall. 1981;29:259.

22 Svoboda J, Riedel H. New solutions describing the formation of interparticle necks in solid-state sintering. Acta Metall Mater. 1995;43:1-10.

23 Exner HE. Neck shape and limiting GBD/SD ratios in solid state sintering. Acta Metall. 1987;35:587-597.

24 Bouvard D, McMeeking RM. Deformation of interparticle necks by diffusion-controlled creep. J Am Ceram Soc. 1996;79:666-672.

25 Pan J, Cocks ACF. A numerical technique for the analysis of coupled surface and grain-boundary diffusion. Acta Metall Mater. 1995;43:1395-1406.

26 Zhang W, Schneibel JH. The sintering of two particles by surface and grain boundary diffusion-A two dimensional numerical study. Acta Metall Mater. 1995;43:4377-4386.

27 Zhang W, Gladwell I. Sintering of two particles by surface and grain boundary diffusion- a three-dimensional model and a numerical study. Comp Mater Sci 1998;12:84-104.
28 Djohari H, Derby JJ. Transport mechanisms and densification during sintering: II. Grain boundaries. Chem Eng Sci. 2009;64:3810-3816.
29 Bruchon J, Pino-Muñoz D, Valdivieso F, Drapier S. Finite element simulation of mass transport during sintering of granular packing. Part I. Surface and lattice diffusion. J Am Ceram Soc. 2012;95:2398-2405.
30 Luo W, Pan J. Effects of surface diffusion and heating rate on first-stage sintering that densifies by grain-boundary diffusion. J Am Ceram Soc. 2015;98:3483-3489.
31 Tikare V, Braginsky M, Olevsky EA. Numerical simulation of solid-state sintering: I, Sintering of three particles. J Am Ceram Soc. 2003;86:49-53.
32 Mori K, Matsubara H, Noguchi N. Micro-macro simulation of sintering process by coupling Monte Carlo and finite element methods. Int J Mech Sci. 2004;46:841-854.
33 Cardona CG, Tikare V, Patterson BR, Olevsky E. On sintering stress in complex powder compacts. J Am Ceram Soc. 2012;95:2372-2382.

34 Bjørk R, Tikare V, Frandsen HL, Pryds N. The effect of particle size distribution on the microstructural evolution during sintering. J Am Ceram Soc. 2013;96:103-110.
35 Wang YU. Computer modeling and simulation of solid-state sintering: A phase field approach. Acta Mater. 2006;54:953-961.
36 Asp K, Ågren J. Phase-field simulation of sintering and related phenomena – A vacancy diffusion approach. Acta Mater. 2006;54:1241-1248.
37 Shinagawa K. Simulation of grain growth and sintering process by combined phase-field/discrete-element method. Acta Mater. 2014;66:360-369.
38 Jagota A, Dawson PR. Micromechanical modeling of powder compacts-II. Truss formulation of discrete packings. Acta Metall. 1988;36:2563-2573.
39 Mori K, Ohashi M, Osakada K. Simulation of microscopic shrinkage behavior in sintering of powder compact. Int J Mech Sci. 1998;40:989-999.
40 Luding S, Manetsberger K, Müllers J. A discrete model for long time sintering. J Mech Phys Solid. 2005;53:455-491.
41 Parhami F, McMeeking RM. A network model for initial stage sintering. Mech Mater. 1998;27:111-124.
42 Martin CL, Schneider LCR, Olmos L, Bouvard D. Discrete element modeling of metallic powder sintering. Scr Mater. 2006;55:425-428.

43 Henrich B, Wonisch A, Kraft T, Moseler M, Riedel H. Simulation of the influence of rearrangement during sintering. Acta Mater. 2007;55:753-762.
44 Brakke KA. The Surface Evolver. Exp Math. 1992;1:141-165.
45 Wakai F. Modeling and simulation of elementary processes in ideal sintering. J Am Ceram Soc. 2006;89:1471-1484.
46 Okuma G, Kadowaki D, Hondo T, Tanaka S, Wakai F. Interface topology for distinguishing stages of sintering. Sci. Rep. 2017;7:11106.
47 Mullins WW. Theory of thermal grooving. J Appl Phys. 1957;28:333-339.
48 Cahn JW, Taylor JE. Surface motion by surface diffusion. Acta Metall Mater. 1994;42:1045-1063.
49 Herring C. Effect of change of scale on sintering phenomena. J Appl Phys. 1950;21:301-303.
50 Kellett BJ, Lange FF. Thermodynamics of densification: I, Sintering of simple particle arrays, equilibrium cofigurations, pore stability, and shrinkage. J Am Ceram Soc. 1989;72:725-734.
51 Wakai F, Aldinger F. Equilibrium configuration of particles in sintering under constraint. Acta Mater. 2003;51:641-652.
52 Coblenz WS, Dynys JM, Canon RM, Coble RL. Initial stage solid state sintering models, In: Kuczynski GC ed. Materials Science Research, vol. 13, Plenum Press; 1980; p. 141-157.

53 Nichols FA, Mullins WW. Morphological changes of a surface of revolution due to capillary-induced surface diffusion. J Appl Phys. 1965;36:1826-1835.
54 Nichols FA. Coalescence of two spheres by surface diffusion. J Appl Phys. 1966;37:2805-2808.
55 German RM, Lathrop JF. Simulation of spherical powder sintering by surface diffusion. J Mater Sci. 1978;13:921-929.
56 Gregg RA, Rhines FN. Surface tension and the sintering force in copper. Metall Trans. 1973;4:1365-1374.
57 Cundall PA, Strack ODL. A discrete numerical model for granular assemblies. Géotechnique. 1979;29:47-65.
58 Martin CL, Bordia RK. Acta Mater. 2009;57:549-558.
59 Martin CL, Yan Z, Jauffres D, Bouvard D, Bordia RK. Sintered ceramics with controlled microstructures: numerical investigations with the Discrete Element Method. J Ceram Soc Japan. 2016;124:340-345.
60 Wakai F, Aldinger F. Sintering through surface motion by the difference in mean curvature. Acta Mater. 2003;51:4013-4024.
61 Wakai F, Gómez-Garcia D, Domínguez-Rodríguez A. Pore channel closure in sintering of a ring of three spheres. J Euro Ceram Soc. 2007;27:3365-3370.
62 Wakai F, Brakke KA. Tensor virial equation of evolving surfaces in sintering of aggregates of particles by diffusion. Acta Mater. 2013;61:4103-4112.

63 Klinger L, Rabkin E. Sintering of spherical particles of two immiscible phases controlled by surface and interphase boundary diffusion. Acta Mater. 2013;61:2607-2616.
64 Missiaen J-M, Lebrun J-M. A new closed-form model for solid-state sintering kinetics. J Am Ceram Soc. 2015;98:3460-3468.

Figure caption

Fig. 1 Sintering of a ring of three spheres by coupled grain boundary diffusion and surface diffusion ($\delta D_{gb}/\delta D_s$ = 1, γ_{gb}/γ_s = 0.5 (ψ = 151°)). (a) Dimensionless time t^* = 1.2 × 10^{-5}, effective contact radius c^*/r_0 = 0.30, (b) t^* = 5.8 × 10^{-5}, c^*/r_0 = 0.39, (c) t^* = 0.00020, c^*/r_0 = 0.47, (d) t^* = 0.00037, c^*/r_0 = 0.53, (e) t^* = 0.0071, c^*/r_0 = 0.72. The upper part shows the process of pore channel pinch-off. The lower part shows the distribution of normal stress σ_n on a grain boundary.

Fig. 2 Normalized energy per particle as a function of dimensionless time. The equilibrium shapes with the minimal energy are shown as examples.

Fig. 3 Effective contact radius as a function of dimensionless time. (a) Effect of γ_{gb}/γ_s, (b) Effect of $\delta D_{gb}/\delta D_s$. Arrows show pore channel pinch-off. The slope shows the exponent $m = 6$ in Eq. (24) for sintering by grain boundary diffusion and surface diffusion.

Fig. 4 Relationship between geometry factor and effective contact radius. Some examples of contact shape for γ_{gb}/γ_s = 0 are shown in the figure.

Fig. 5 Relation between weighted average of curvature and effective contact radius. (a) Effect of γ_{gb}/γ_s, (b) Effect of $\delta D_{gb}/\delta D_s$.

Fig. 6 Relation between sintering force and effective contact radius. (a) Effect of γ_{gb}/γ_s, (b) Effect of $\delta D_{gb}/\delta D_s$.

Fig. 7 Relation between relative velocity and effective contact radius.

Fig. 8 Shrinkage as a function of the dimensionless time. Solid line represents the distance between mass centers ΔR. Broken line represents the rigid body motion $\boldsymbol{u}$ caused by grain boundary diffusion.

Fig. 9 Piece-wise linear approximation of sintering force.

Fig. 10 Configuration of spheres at the pinch-off. For the pore coordination number $n=3$, θ is 30° and c/r_0 is 0.5.

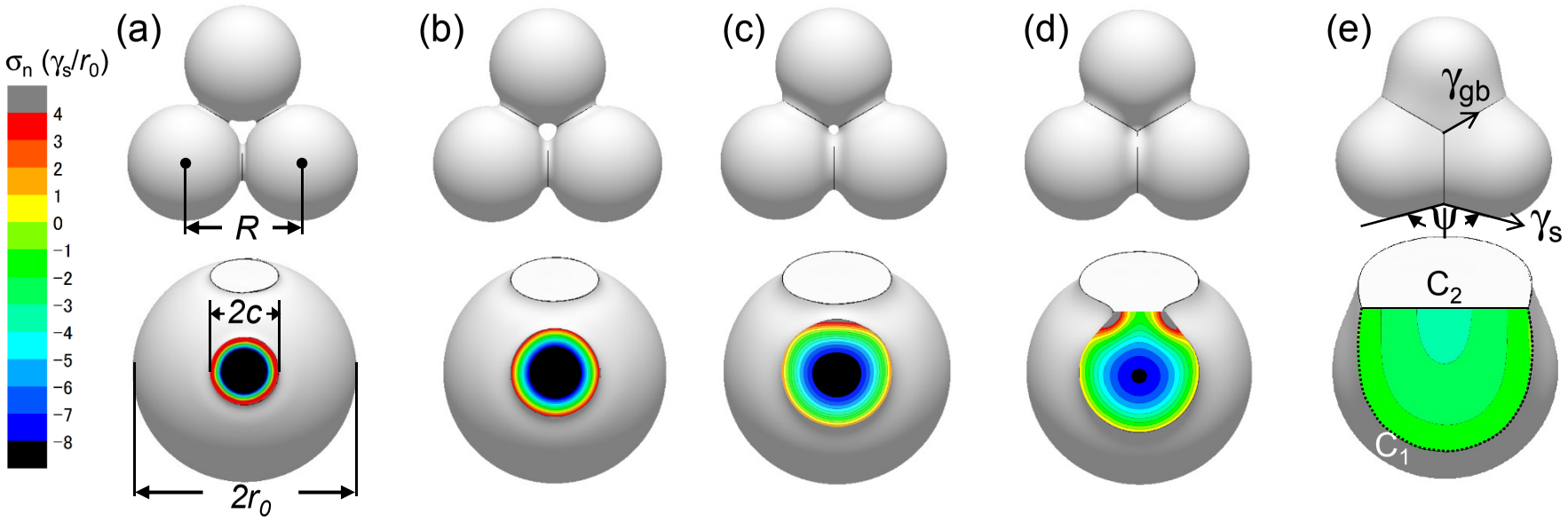

Fig. 1 Sintering of a ring of three spheres by coupled grain boundary diffusion and surface diffusion ($\delta D_{gb}/\delta D_s$ = 1, γ_{gb}/γ_s = 0.5 (ψ = 151°)). (a) Dimensionless time t^* = 1.2 × 10^{-5}, effective contact radius c^*/r_0 = 0.30, (b) t^* = 5.8 × 10^{-5}, c^*/r_0 = 0.39, (c) t^* = 0.00020, c^*/r_0 = 0.47, (d) t^* = 0.00037, c^*/r_0 = 0.53, (e) t^* = 0.0071, c^*/r_0 = 0.72. The upper part shows the process of pore channel pinch-off. The lower part shows the distribution of normal stress σ_n on a grain boundary.

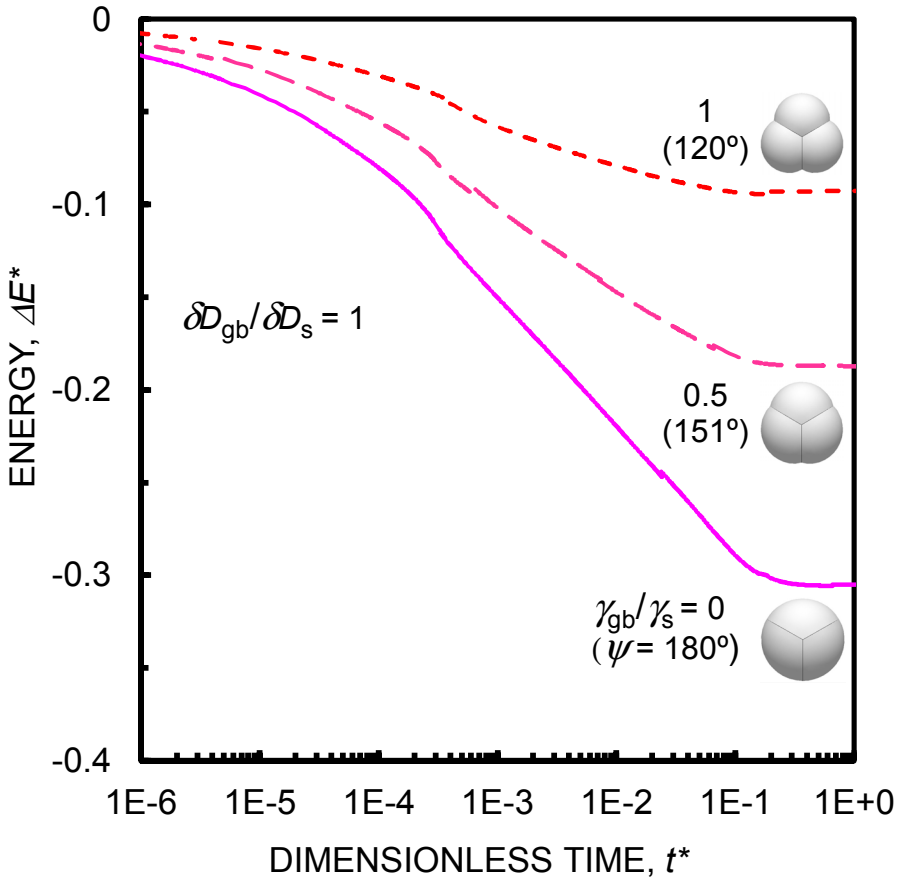

Fig. 2 Normalized energy per particle as a function of dimensionless time. The equilibrium shapes with the minimal energy are shown as examples.

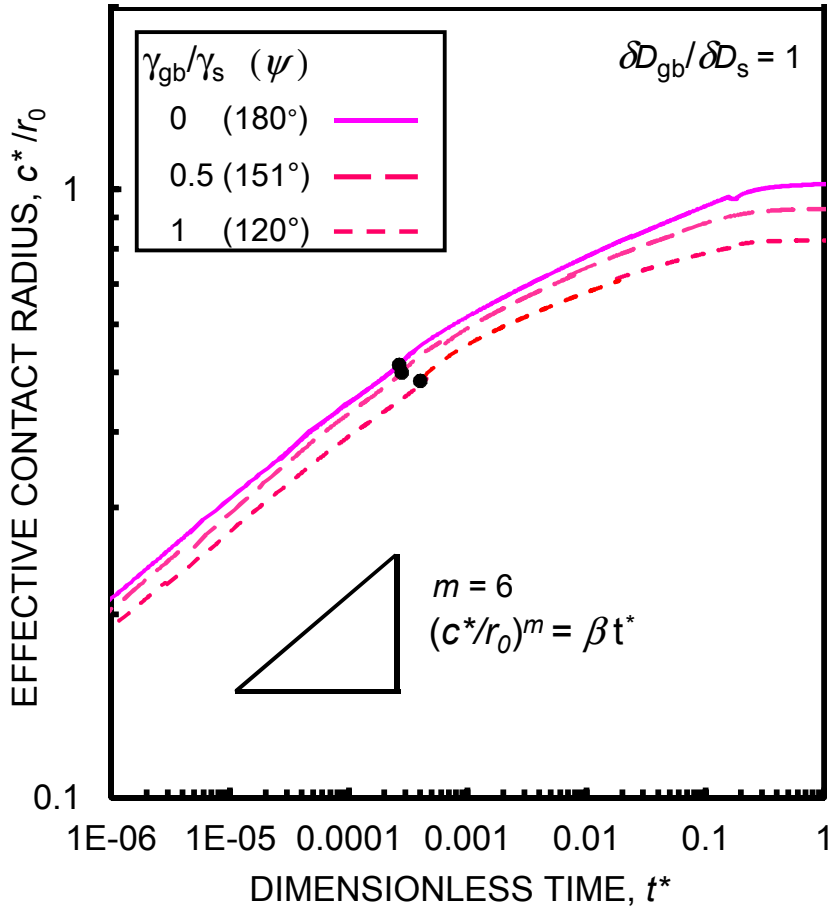

Fig. 3 Effective contact radius as a function of dimensionless time. (a) Effect of γ_{gb}/γ_s. Arrows show pore channel pinch-off. The slope shows the exponent $m = 6$ in Eq. (24) for sintering by grain boundary diffusion and surface diffusion.

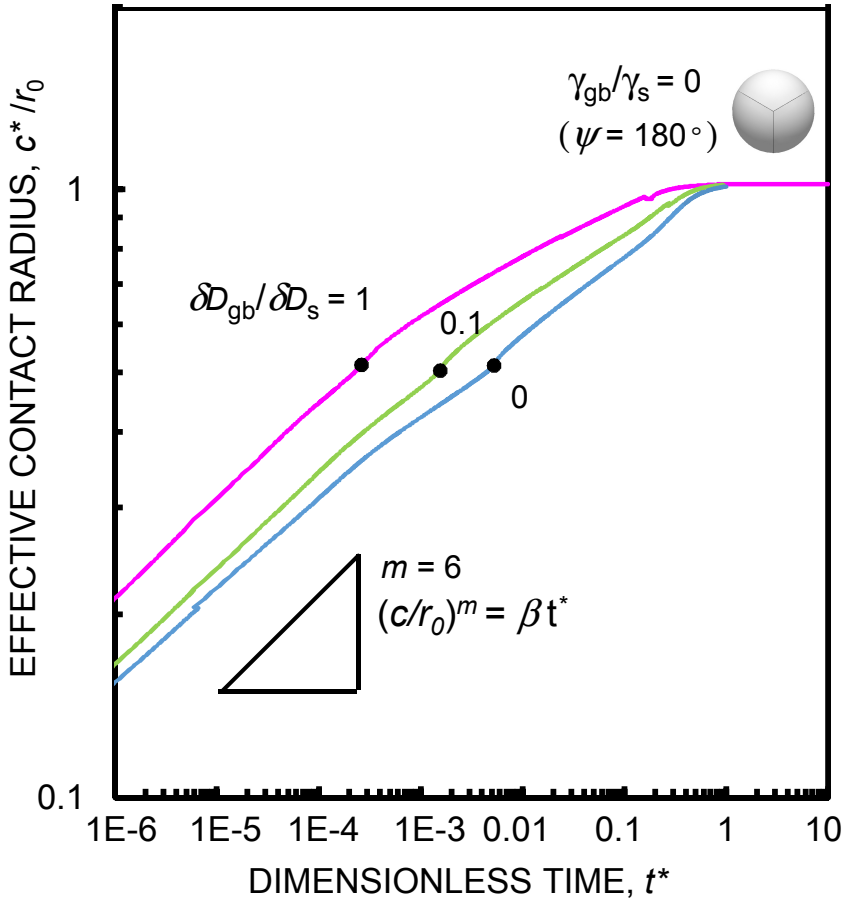

Fig. 3 Effect of contact radius as a function of dimensionless time. (b) Effect of $\delta D_{gb}/\delta D_s$. Arrows show pore channel pinch-off. The slope shows the exponent $m = 6$ in Eq. (24) for sintering by grain boundary diffusion and surface diffusion.

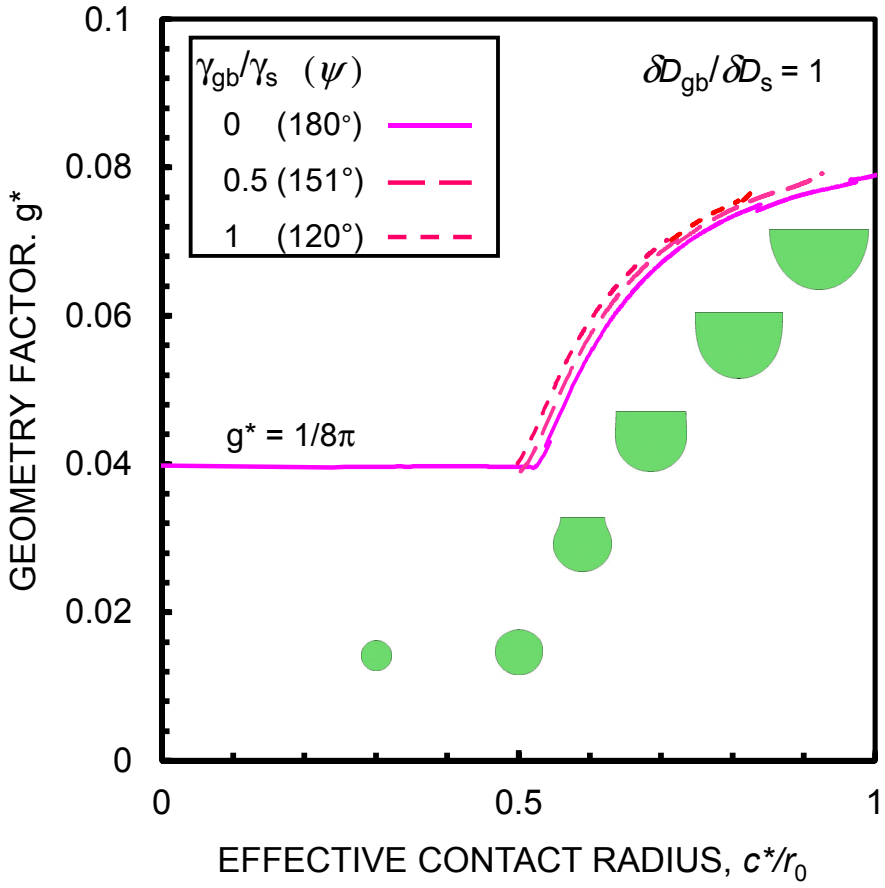

Fig. 4 Relationship between geometry factor and effective contact radius. Some examples of contact shape for γ_{gb}/γ_s = 0 are shown in the figure.

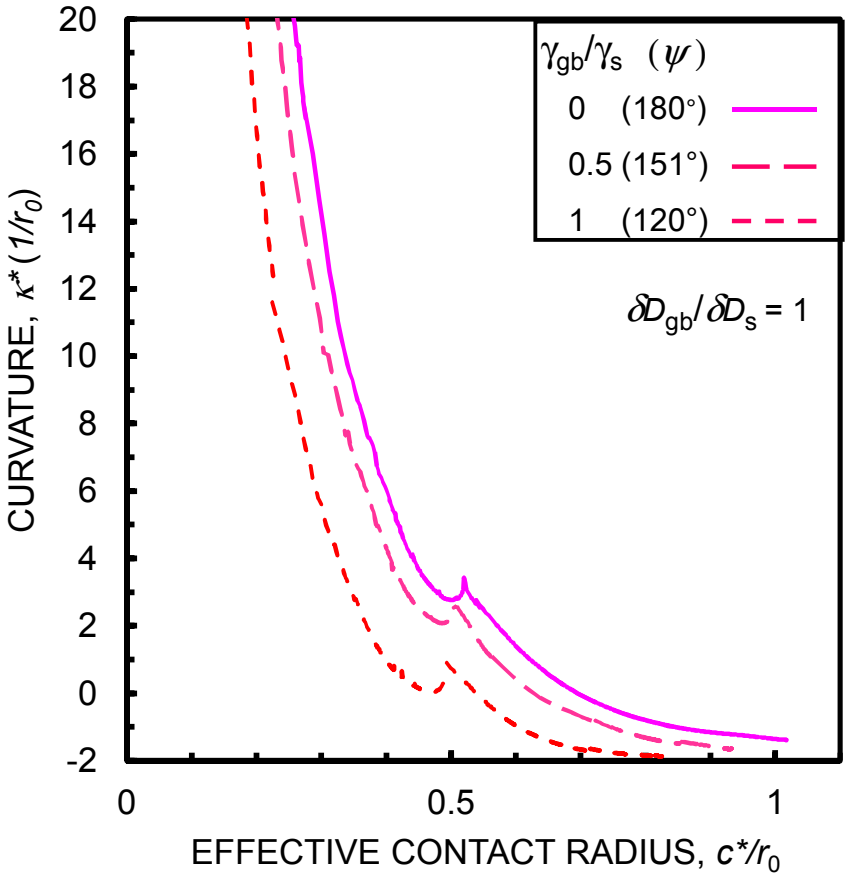

Fig. 5 Relation between weighted average of curvature and effective contact radius. (a) Effect of γ_{gb}/γ_s.

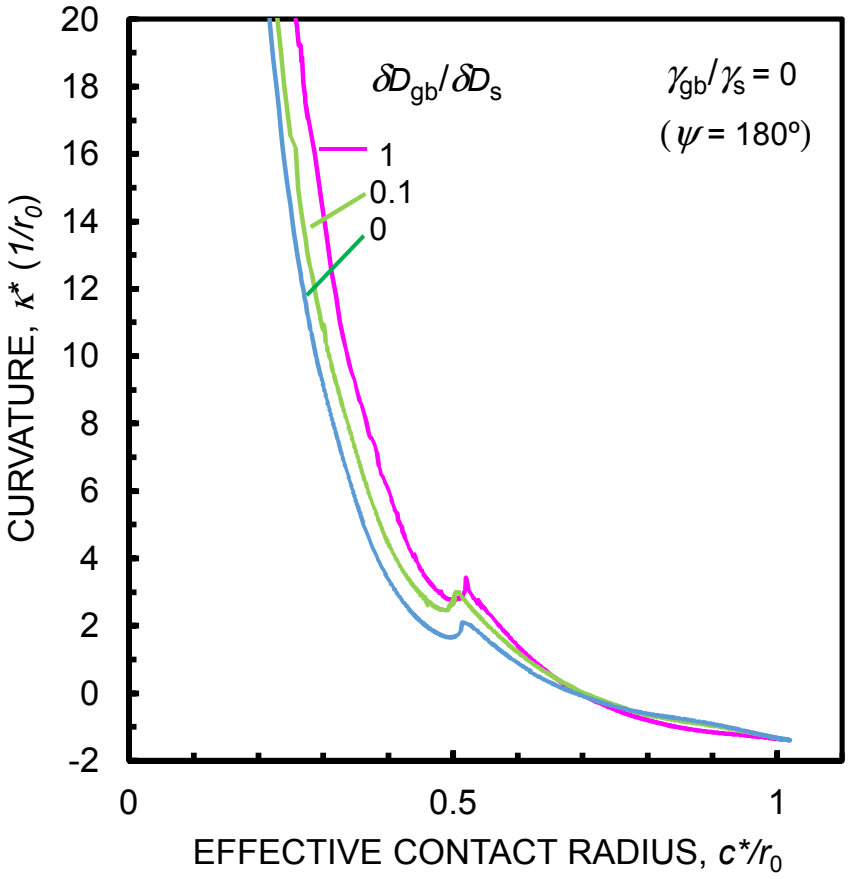

Fig. 5 Relation between weighted average of curvature and effective contact radius. (b) Effect of $\delta D_{gb}/\delta D_s$.

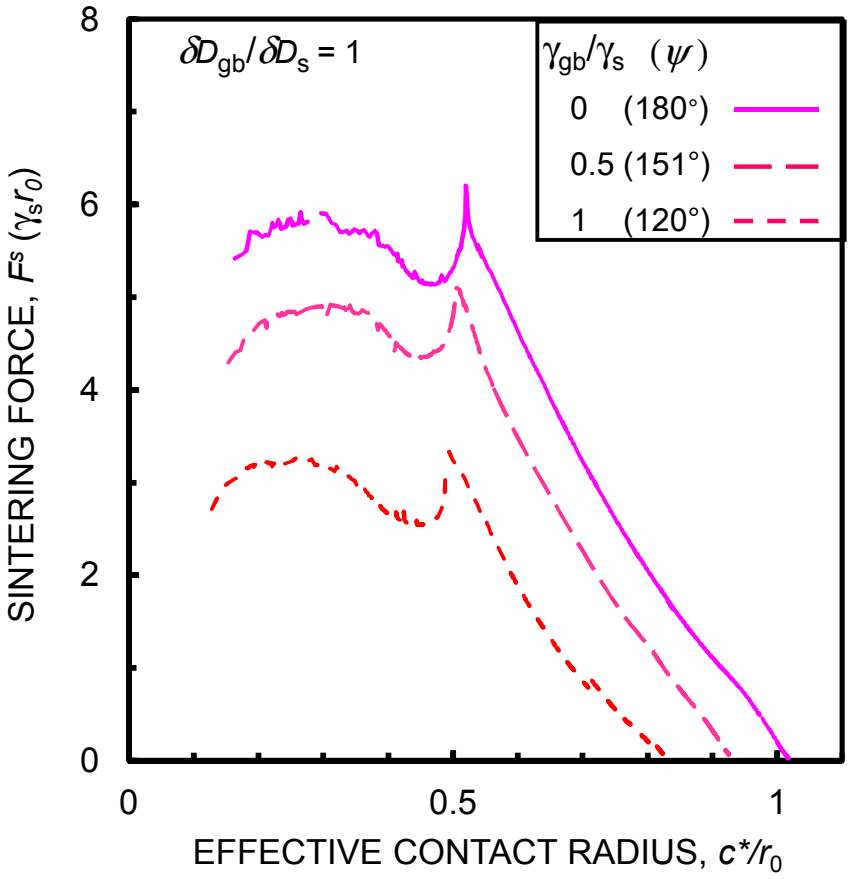

Fig. 6 Relation between sintering force and effective contact radius. (a) Effect of γ_{gb}/γ_s.

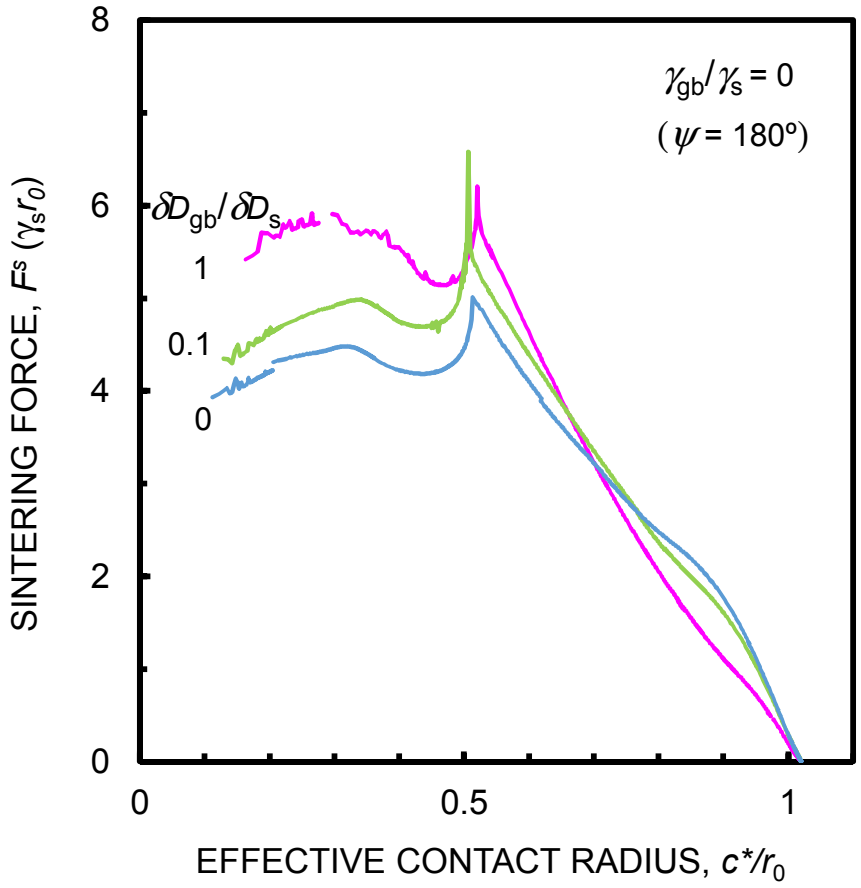

Fig. 6 Relation between sintering force and effective contact radius. (b) Effect of $\delta D_{gb}/\delta D_s$.

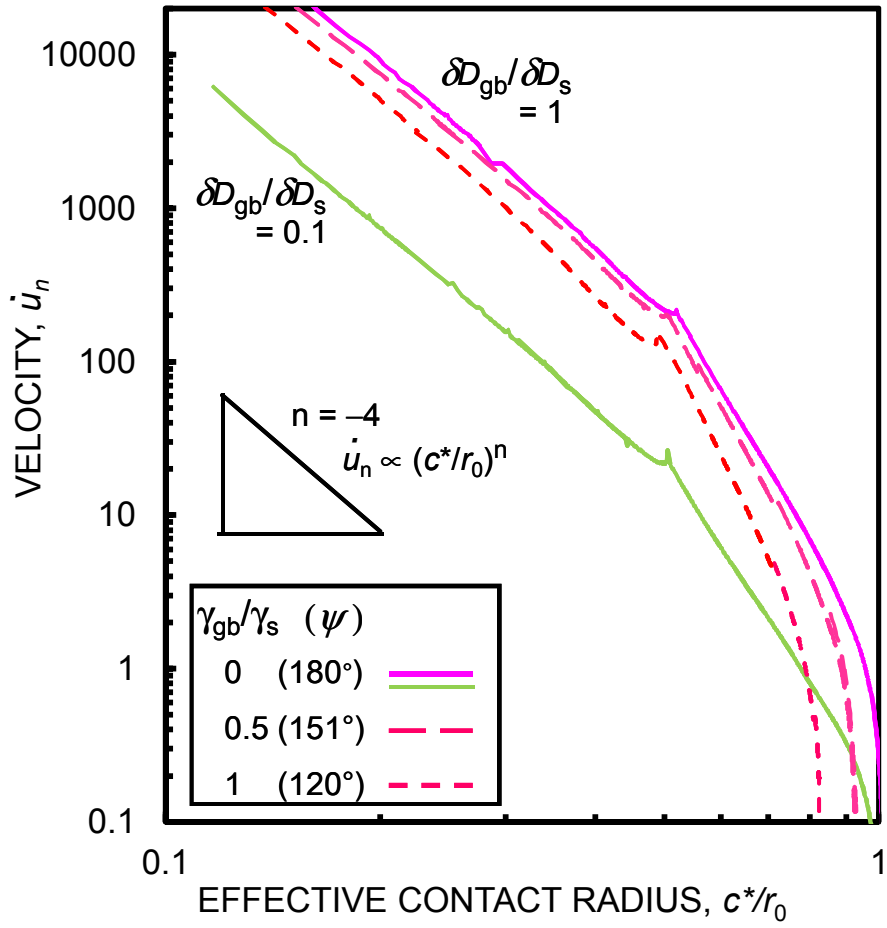

Fig. 7 Relation between relative velocity and effective contact radius.

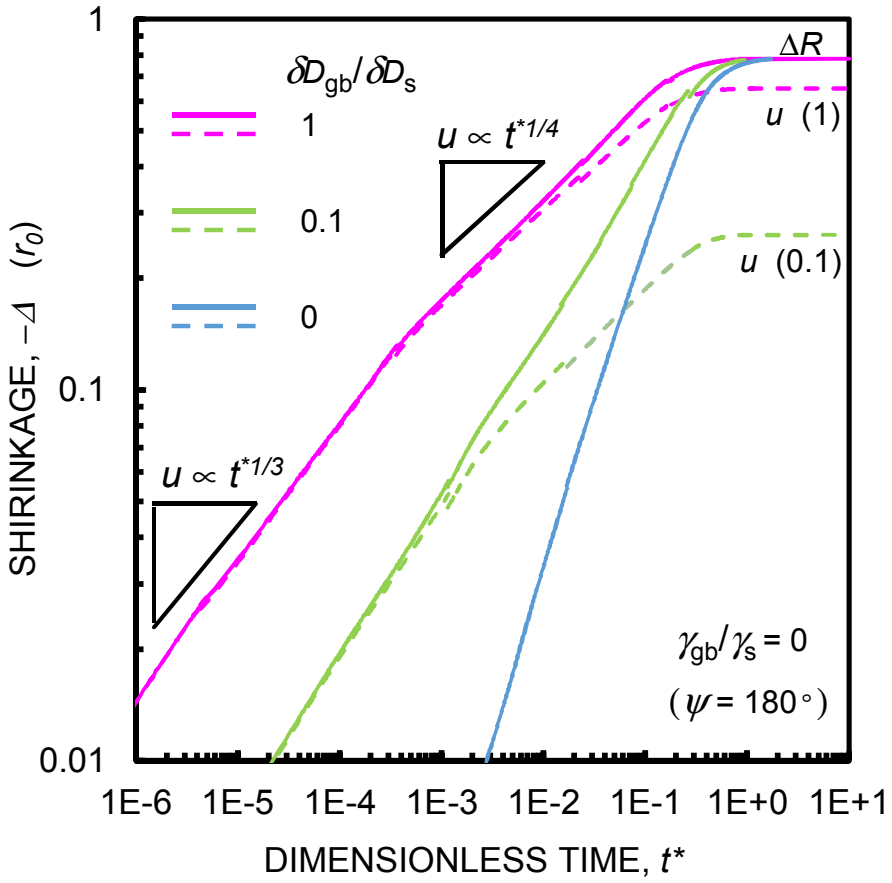

Fig. 8 Shrinkage as a function of the dimensionless time. Solid line represents the distance between mass centers ΔR. Broken line represents the rigid body motion u caused by grain boundary diffusion.

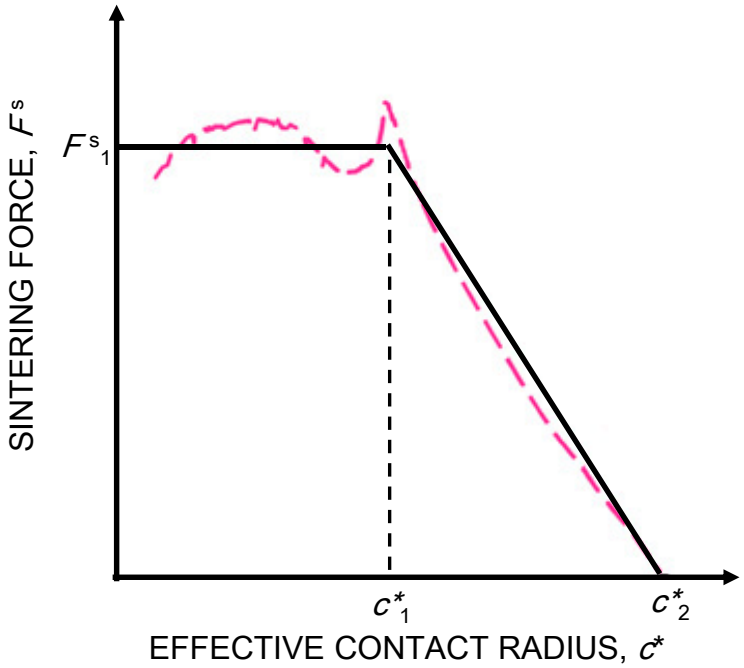

Fig. 9 Piece-wise linear approximation of sintering force.

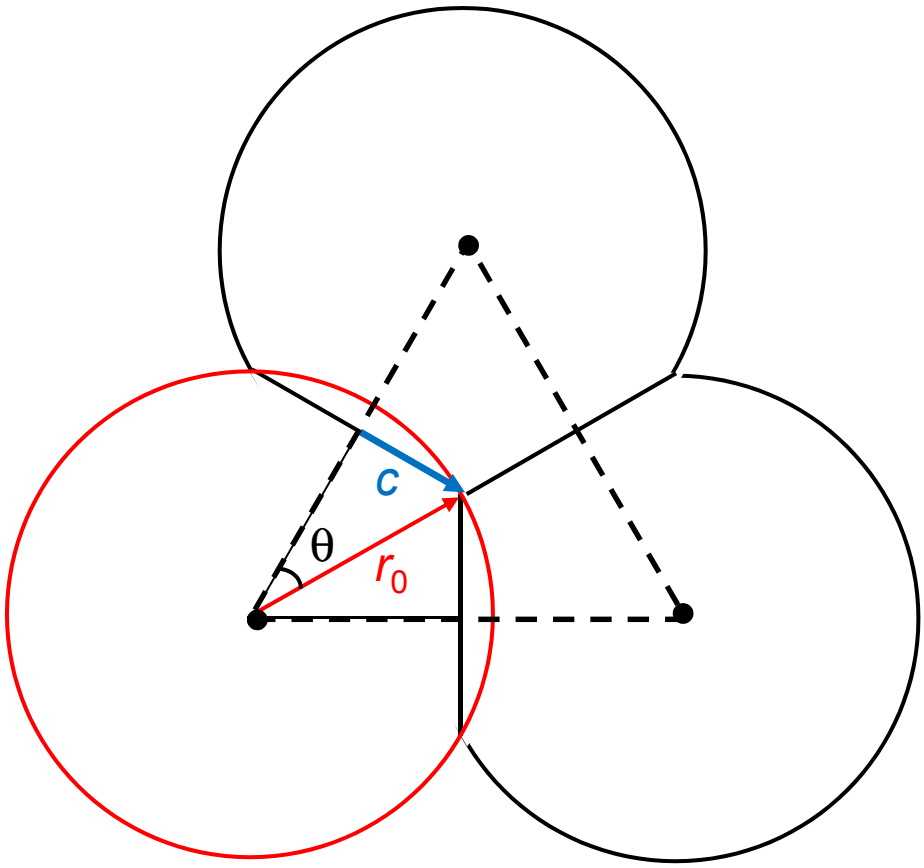

Fig. 10 Configuration of spheres at the pinch-off. For the pore coordination number n = 3, θ is 30° and c/r_0 is 0.5.